

ARTICLE OPEN

Raman detection of hidden phonons assisted by atomic point defects in a two-dimensional semimetal

Hui Yuan¹, Xieyu Zhou², Yan Cao¹, Qi Bian¹, Zongyuan Zhang¹, Haigen Sun¹, Shaojian Li¹, Zhibin Shao¹, Jin Hu³, Yanglin Zhu³, Zhiqiang Mao³, Wei Ji² and Minghu Pan¹

Defects usually have an important role in tailoring various properties of two-dimensional (2D) materials. However, optical detection of defects, especially single-atom point defects, is very challenging in 2D layers. Here, we report our systematic studies on the Raman-activated defect vibrational modes in 2D semimetallic material by combining Raman spectroscopy, density functional theory (DFT) calculation and scanning tunneling microscopy (STM). We observed three common Raman-active vibrational modes located at 95 (A_{1g}^2), 228 (A_{1g}^1), and 304 cm^{-1} (B_{1g}^1) in ZrSiTe few-layers, consistent with our theoretical calculations. Moreover, a pronounced mode sitting at 131.7 cm^{-1} was found in the ZrSiTe monolayer. This mode fades out quickly in the bilayer (2L) and eventually disappears in 4L. The high-resolution STM images and DFT calculations suggest this mode to be an intralayer shear mode at the Brillouin zone boundary which is activated by atomic point defects, and STM-based inelastic tunneling spectrum further confirms the existence of such a defect mode. The appearance of such 'forbidden' modes in Raman spectra may pave an avenue for the optical characterization of single-atom point defects in metallic 2D layers.

npj 2D Materials and Applications (2019)3:12; <https://doi.org/10.1038/s41699-019-0093-7>

INTRODUCTION

Recently, topological nodal line semimetals (TNLSMs) ZrSiX (X = S, Se, and Te) have attracted extensive attention. In TNLSMs, the conduction and valence bands cross at several points in k -space with forming a closed loop on the Fermi surface. These loops are protected by the nonsymmorphic symmetry^{1–3}, and the electronic states along the nodal lines are topologically nontrivial. The crystalline and band structures of ZrSiX have been studied by means of X-ray diffraction⁴ and angle resolved photoemission spectroscopy (ARPES)^{5–7}. The unique band structure of ZrSiX leads to various interesting physical properties, e.g., chiral anomaly, extremely large magnetoresistance, high-carrier mobility with high-carrier density, etc.^{5,8}. Due to the weak interlayer interaction⁹, ZrSiTe shows some two-dimensional (2D) characteristic in its band structure, revealed by quantum oscillation in magnetic susceptibility and magnetoresistance⁸. More interestingly, ZrSiTe was theoretically predicted to be a topological insulator when it is thinned down to the monolayer limit^{1,9,10}. Although the physical properties of bulk ZrSiTe have been studied extensively, those of mono- and few-layers are still unclear.

For most 2D materials such as graphene, transition metal dichalcogenides (TMDs), and black phosphorus (BP), Raman spectroscopy provide a powerful tool to investigate the evolution of crystalline symmetry and interlayer interactions during a thinning down process^{11–21}. Defects in 2D materials may induce a shift in frequency and an asymmetrical broadening of Raman peaks^{22,23}. In addition, line defects, e.g., phonons at layer edges, can also be detected in black phosphorus²⁴ and MoS₂²⁵ by polarized Raman spectroscopy. However, the momentum

conservation rule requires $q \approx 0$ for a Raman process, thus phonon modes away from the Γ point in the q -space are hardly involved in a sole Raman scattering process²⁶. For example, Hong et al.²⁷ studied point-like defects in monolayer MoS₂ and obtained nearly-perfect Raman spectra without showing any signature of defects, whereas the sample shows plenty of point defects in scanning transmission electron microscopic (STEM) images. Although it was recently demonstrated that photoluminescence (PL) might be another feasible method for detecting single-atom point defects^{28,29}, it was designed for semiconductors and does not work for (semi-) metals. It therefore remains a huge challenge to quickly detect single-atom point defects using optical methods, especially in metallic, layered materials.

In this work, mono- to few-layered ZrSiTe films were exfoliated on a 285 nm-thick SiO₂/Si substrate with the Scotch tape method. A systematic Raman study was performed in order to investigate the layer-dependent lattice vibration properties. Our results show significant thickness dependences of Raman peak position and intensity in ZrSiTe mono- and few-layers. In all thicknesses, three major Raman modes (around 95 (A_{1g}^2), 228 (A_{1g}^1), and 304 cm^{-1} (B_{1g}^1)) and three minor modes are identified. Raman-active vibrational modes of 2D ZrSiTe were also modeled with density functional theory (DFT) calculations. All experimental observed modes except for the one located at 131.7 cm^{-1} are found to be the intrinsic vibration modes related to the crystal symmetry of ZrSiTe by our DFT calculations. The 131.7 cm^{-1} mode does not exist in the list of Raman-active modes predicted by the calculation of defect-free layers but can be understood as a combination of the intralayer shear modes at the Brillouin zone

¹School of Physics, Huazhong University of Science and Technology, 1037 Luoyu Road, 430074 Wuhan, Hubei, China; ²Department of Physics and Beijing Key Laboratory of Optoelectronic Functional Materials & Micro-Nano Devices, Renmin University of China, 100872 Beijing, China and ³Department of Physics and Engineering Physics, Tulane University, New Orleans, LO 70118, USA

Correspondence: Wei Ji (wj@ruc.edu.cn) or Minghu Pan (minghupan@hust.edu.cn)

These authors contributed equally: Hui Yuan, Xieyu Zhou, Yan Cao

Received: 19 September 2018 Accepted: 20 February 2019

Published online: 11 March 2019

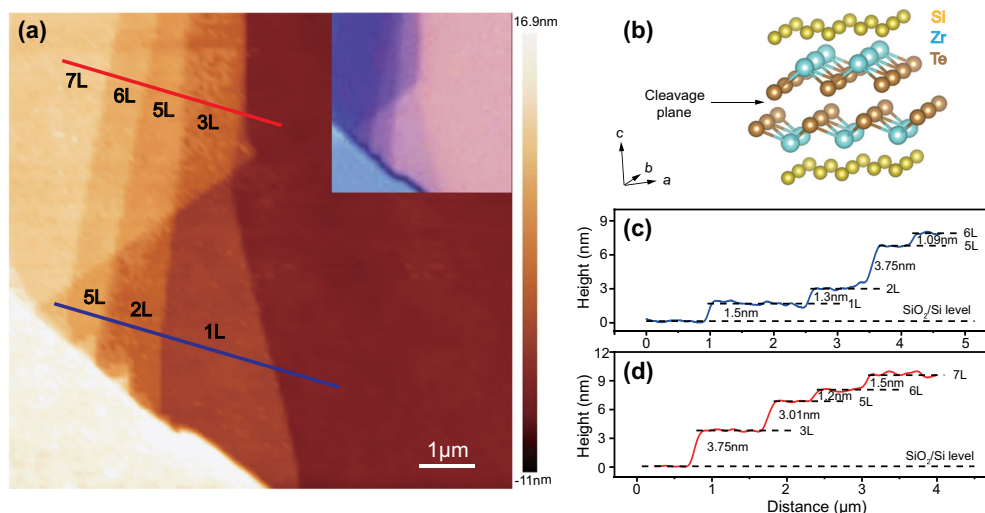


Fig. 1 Topology of a typical ZrSiTe flake on a 285 nm SiO₂/Si substrate. **a** The optical (the inset of **a**) and AFM images of a ZrSiTe flake on a 285 nm SiO₂/Si substrate. The length of the scale bar is 1 μm. The variation of the thickness can be identified layer-by-layer both in optical and AFM topography images. **b** Crystalline structure of ZrSiTe. The cleavage plane between adjacent Te layers is indicated by an arrow. The line profile shown in **c** and **d** indicates the height profile along the blue and red solid line, respectively. The dashed lines indicate the average height of the corresponding plane of the layers. The thickness of a single layer can be estimated to be 1.3 nm from these line profiles

(BZ) boundary activated in thin layers. In long-stored samples, the defect-induced localized modes around 120 cm⁻¹ also contribute to the 131.7 cm⁻¹ mode and induce a red-shift of it. The total intensity of this mode can be further enhanced by 4.8 times upon increasing defect concentration.

RESULTS AND DISCUSSION

ZrSiTe has a crystalline structure in the tetragonal PbCl₂ type (*P4/nmm* space group No. 129)^{4,5,9,30}. In the lattice of ZrSiTe, double layers of Zr–Te are separated by a layer of a Si square net. Two adjacent Te layers (Fig. 1b) are expected to be separated upon a cleavage along the (001)-orientation. Compared to its analogues, ZrSiS and ZrSiSe, the interlayer interactions in ZrSiTe are much weaker, evoking the possibility of isolating ZrSiTe monolayers from its bulk crystals by mechanical cleavage^{8,9}. As a result, the thickness-dependent evolution of ZrSiTe lattice structure and physical properties could be studied with a layer-by-layer resolution. Figure 1a shows a typical atomic force microscopic (AFM) image and the corresponding optical image (inset of Fig. 1a) of the ZrSiTe mono- to few-layers, deposited on a 285 nm-thick SiO₂/Si substrate. The ZrSiTe monolayer is light purple and the color quickly gets darker as the thickness of ZrSiTe gets larger from 2 to 6 layers. Then, the color of ZrSiTe film turns blue, green, beige and golden with respect to the increasing thicknesses. Similar color codes have also been found in TMDs such as MoS₂, MoTe₂ and WTe₂^{15,18,31,32}, suggesting that the color of ZrSiTe on the SiO₂/Si substrate is a good indicator of its thickness. The height profile (Fig. 1c, d) measured along the solid line marked in Fig. 1a indicates that the thickness of a single layer is 1.3 nm. This thickness value is slightly larger than the theoretical value 9.5 Å revealed by our DFT calculation for the bulk crystal, but is still reasonable¹⁶. In addition, the monolayer thickness of 1.5 nm is slightly larger than the interlayer distance of ZrSiTe. This phenomenon is usually observed in AFM measurements on exfoliated 2D materials, such as graphene³³, MoS₂^{15,34,35}, and other dichalcogenides¹⁸.

Figure 2a compares the Raman spectra of freshly-cleaved ZrSiTe thin films of various thicknesses, in which the position and intensity of Raman signals consistently vary with the thickness. The sharpest peak is around 228 cm⁻¹ (*A*_{1g}¹) in all samples except the monolayer one. Both this peak and the one around

304 cm⁻¹ (*B*_{1g}¹), are symmetric and can be fitted with single Lorentzian peaks, indicating the absence of strong electron–phonon and spin–phonon couplings in these phonon modes. Our DFT calculations reveal the details of these three observed Raman-active modes. Figure 2e–g illustrates the lattice vibration displacements of these three Raman-active modes at 96.9 (*A*_{2g}²), 226.4 (*A*_{1g}¹), and 299.5 cm⁻¹ (*B*_{1g}¹) in a ZrSiTe bilayer, respectively. All of them are out-of-plane vibration modes.

As shown in Fig. 2b, two Raman modes, i.e., *A*_{1g}¹ and *B*_{1g}¹, are significantly stiffened in thicker samples while the *A*_{1g}¹ mode slightly softens. Layer-dependent frequency shifts of Raman modes were frequently reported in other 2D materials^{11–15,17–21,31,32}. According to our DFT calculations, all these three modes are assigned to out-of-plane vibrations (Fig. 2e–g). While it is straightforward that the stiffening of modes *A*_{2g}² and *B*_{1g}¹ with respect to increasing sample thickness is ascribed to stronger interlayer interactions in thicker layers, the softening of the *A*_{1g}¹ mode is rather complicated. This mode mainly represents the out-of-plane vibrations of Zr atoms, which is influenced by the neighboring surface Te atoms, which weakens with the increase of thickness, are significant in varying vibrational frequencies^{36,37} of 2D materials. These surface Te atoms lead to appreciable softening of the *A*_{1g}¹ mode in ZrSiTe with thickness from 1L to 4L, and the softening becomes not significant above 4L, as shown in Fig. 2a. Table 1 summarizes the experimental and theoretical frequencies of the Raman-activated modes in 1L to 4L ZrSiTe. All experimental frequencies were well reproduced by the theoretical calculations within an error of 3%, indicating the reliability of the DFT calculations. An exception lies in the *A*_{2g}² mode in the monolayer, where the experimental frequency is 4.5% higher than the theoretical value. It is worth noting that in thicker samples, e.g. 4L, more Raman modes could be observed. And the numbering of modes based on their phonon energies may vary. In this manuscript, however, we use the labeling of modes in the bilayer ZrSiTe for all thicknesses for convenience. In addition to the peak position shifts, the overall intensity of Raman signals gets lower if the layer thickness increases, which is most likely ascribed to stronger light absorption in thicker ZrSiTe layers. In fact, it is difficult to acquire effective Raman signals in ZrSiTe samples thicker than 100 nm. The spectrum shown in Fig. 2a is measured from a roughly 50 nm-thick film, denoted as a bulk result.

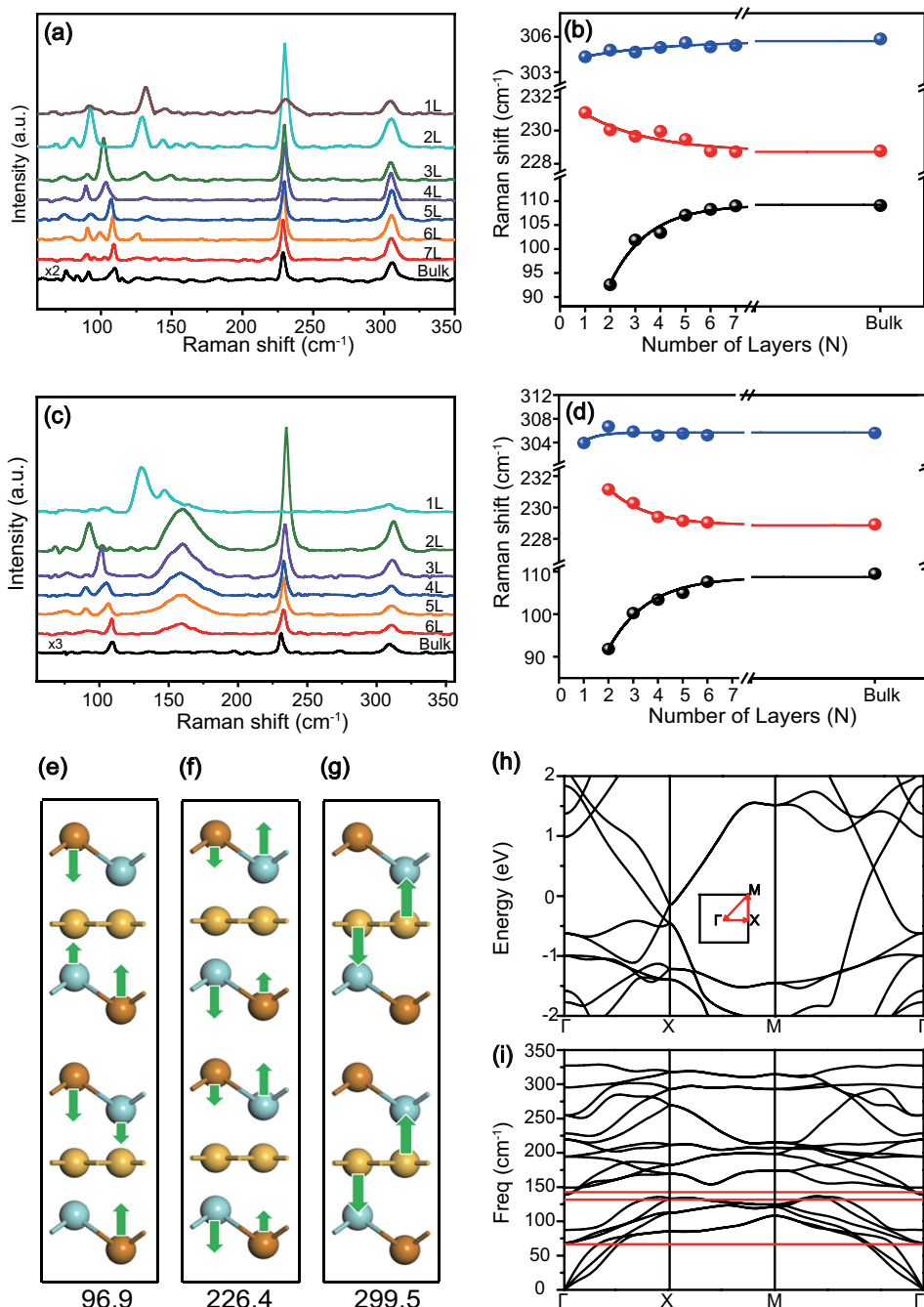


Fig. 2 Layer-dependent Raman spectra and phonon vibration modes in ZrSiTe. **a** The Raman spectra of fresh ZrSiTe with thickness ranging from 1L to bulk ZrSiTe and **b** the evolution of the representative Raman peak positions. The Raman modes in the monolayer ZrSiTe are distinct from the modes in the thicker ones. The sharpest mode in monolayer is at 131.7 cm^{-1} instead of around 228 cm^{-1} as in thicker layers. **c** The Raman spectra of ZrSiTe with various thickness after one-week storage in nitrogen gas-filled glove box, and **d** the representative Raman peak shifts. The Raman modes changed markedly in both monolayer and few layers. The modes at 131.7 and 142.7 cm^{-1} were enhanced in the monolayer, and the wave packet around 150 cm^{-1} arose in few layers. **e–g** The three representative eigen lattice vibration modes in 2L confirmed by the first-principle calculations. **h, i** The electronic and the phonon band structures of the monolayer ZrSiTe. The calculations were performed with considering spin–orbit coupling (SOC). The illustration in **h** shows the Brillouin zone and the path of high symmetry points. The three red horizontal lines in **i** represent the frequency of 66.7 , 131.7 , and 142.7 cm^{-1}

It is worth to note that the Raman spectrum of the ZrSiTe monolayer is distinct from those of other thicknesses. In the monolayer, the strongest mode is centered at 131.7 cm^{-1} instead of 304 cm^{-1} . This mode fades out with respect to the increasing layer thickness, and cannot be clearly observed in the samples thicker than 3L. According to the DFT calculations, this mode is not supposed to be Raman-active in ideal defect-free ZrSiTe

monolayers. It was reported that tellurium thin films show two representative Raman modes at 120 and 140 cm^{-1} , respectively^{38–40}. However, the peak position of the mode at 131.7 cm^{-1} we found in ZrSiTe is appreciably away from the frequencies of both tellurium modes. In addition, the two representative tellurium modes can be observed in all thicknesses, inconsistent with the fact that the 131.7 cm^{-1} mode fades out with increasing

Table 1. Calculated and experimentally energies and symmetries of typical Raman modes in 1 to 4 layer ZrSiTe

1L			2L			3L			4L		
Mode	CAL.	EXPT.									
A_{1g}^2	87.4	91.4	A_{1g}^2	96.9	95.6	A_{1g}^3	86.5	90.2	A_{1g}^4	89.6	89.3
						A_{1g}^2	101.4	101.4	A_{1g}^3	104.6	103.4
									A_{1g}^2	220.4	220.7
A_{1g}^1	225.5	230.9	A_{1g}^1	226.4	228.2	A_{1g}^1	226.5	229.2	A_{1g}^1	226.2	230.3
B_{1g}^1	293.2	302.8	B_{1g}^1	299.5	303.9	B_{1g}^2	299.6	301.7	B_{1g}^2	300.1	303.0
						B_{1g}^1	302.4	305.1	B_{1g}^1	302.0	306.5

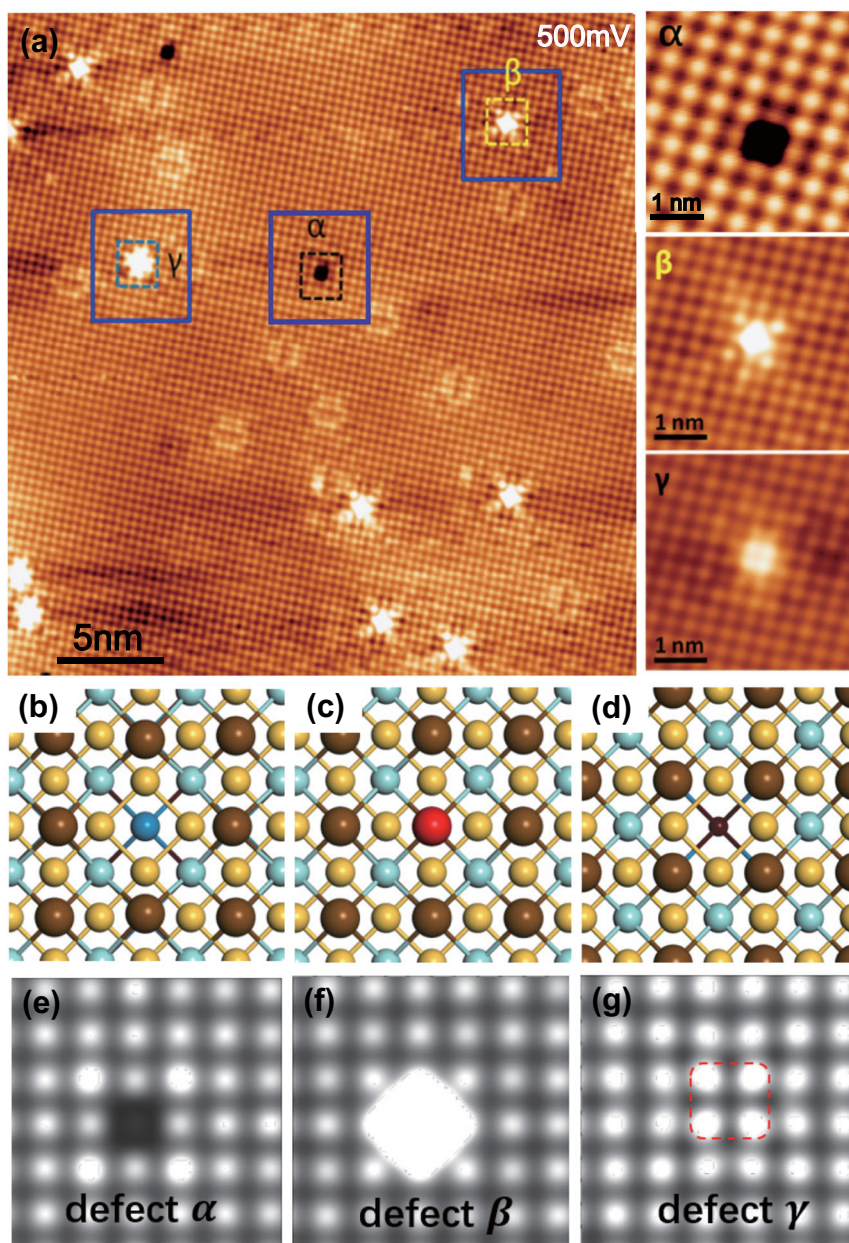


Fig. 3 Topographic STM images for the various surface defects in ZrSiTe. **a** A typical $30 \times 30 \text{ nm}^2$ atom-resolved STM image of in situ exfoliated ZrSiTe surface with defects. The zoom-in of the high-resolution STM image for the defects of types α , β , and γ are shown in the right. The corresponding defects are marked with blue squares in the large image (**a**). The length of the scale bar is 6 nm in the main panel and 1 nm in the right zoom-in panels. **b–d** Top views of the ball-stick models of a 3×3 monolayer ZrSiTe with a Te vacancy, a Te adatom, and a Zr vacancy, respectively. **e–g** Simulated STM images of the defects shown in **b–d**, respectively. Compare **a** with **e–g**, the defect types of α , β , and γ can be evidently ascribed to Te vacancy, Te adatom, and Zr vacancy, respectively

thickness of the ZrSiTe layers. Also, the degraded tellurium is more likely to be amorphous instead of forming the crystal. As a result, the 131.7 cm^{-1} peak observed only in 1L and 2L ZrSiTe samples is unlikely to originate from the modes of α -phase tellurium few-layers. In 2D materials, defects often have significant influences on Raman spectra^{11,12,41}. It is reasonable to infer that the 131.7 cm^{-1} mode in thin layer ZrSiTe samples is related to defects.

We performed scanning tunneling microscopic (STM) measurements on an in situ cleaved ZrSiTe surface. Figure 3a shows a topographic STM image of the cleaved surface. The surface Te lattice was visualized as a bright dot array. The nearest Te–Te distance was measured to be 3.7 \AA , which is consistent with the theoretical value of 3.68 \AA ⁴, suggesting no obvious surface reconstruction occurred during the cleavage. In addition, three types of defects, labeled as α , β , and γ respectively, were clearly observed on the surface. High-resolution STM images of these three types of defects are given in the right panels of Fig. 3a. The α defect appears as a dark hole. The β defect appears as a bright protrusion with a star-like shape. And the γ defect shows a similar bright protrusion with β , but in a square shape. Our statistics show that the β defect, with a concentration of 2.6‰ estimated by counting the number of defects in all scanned areas, is the most common defect on the ZrSiTe surface.

In order to identify these atomic defects, three most probable types of defects, *i.e.* Te vacancy, Te adatom and Zr vacancy, were modeled by our DFT calculations. Figure 3b–d shows the top view of a 3×3 lattice ball-stick model of the ZrSiTe monolayer with these three types of defects. Meanwhile, Fig. 3e–g exhibits the corresponding simulated STM images, which are highly consistent with the experimental images of the α , β , and γ defects, respectively. Moreover, in the tellurium-rich limit, the formation energy is 1.3 eV for the Te adatom, 2.8 eV for the Te vacancy and 3.8 to 4.6 eV for the Zr vacancy. In contrast, in the zirconium-rich (tellurium-deficient) limit, the formation energy is 2.1 to 1.3 eV, 2.0 to 2.8 eV and 4.6 eV for these three types of defects, respectively.

Therefore, the most common β defect is assigned to the Te adatom, because of the high consistency between the simulated and experimental results, and the lowest formation energy. Based on similar derivations, we assess defects α and γ to the Te vacancy and the Zr vacancy, respectively.

In order to further understand the relationship between the Raman signals and the defect related lattice vibration modes of the ZrSiTe layers, we performed density functional perturbation theory (DFPT) calculations for ZrSiTe mono- and few-layers. According to our DFPT results, the 131.7 cm^{-1} mode found in thinner layers is most likely resulted from atomic defects assisted or induced Raman scattering, rather than an eigen-vibrational mode at the Γ point (see Supplementary Information Fig. S1a). It was reported that atomic defects could provide additional inelastic scattering processes, leading to the zone boundary phonons modes being observable in Raman spectra, like the D peak in graphene¹¹. Here, we show the phonon dispersion relation of the ZrSiTe monolayer in Fig. 2i, which indicates a mode with a rather small dispersion along X–M exhibiting a frequency of 133.0 cm^{-1} at the X(0.5,0,0) point on the boundary of the BZ. Figure S2b illustrates the vibrational displacements of this mode, which suggest an intralayer shear vibration inducing rumpling of the layer. This rumpling is activated in thinner layers where the perpendicular interlayer interactions are not stiff enough. It might be squeezed to a nearly in-plane mode when the thickness is significantly large, resulting in severely depressed Raman signals around 130 cm^{-1} in thicker layers (Fig. 2a). Similarly, some ‘forbidden’ modes can be also observed in the 2D materials with the CdI₂ crystal structure (e.g., HfS₂, SnS₂, PtSe₂)^{25,42–46}. However, unlike defect-induced Raman modes in our case, they are infrared-active modes or secondary-order Raman modes presented in the spectra owing to resonant Raman scattering. We also found several localized modes caused by defects in the adjacent frequency range (Fig. S2 and S3). Thus, the 131.7 cm^{-1} peak could be a combined signal of those adjacent localized modes

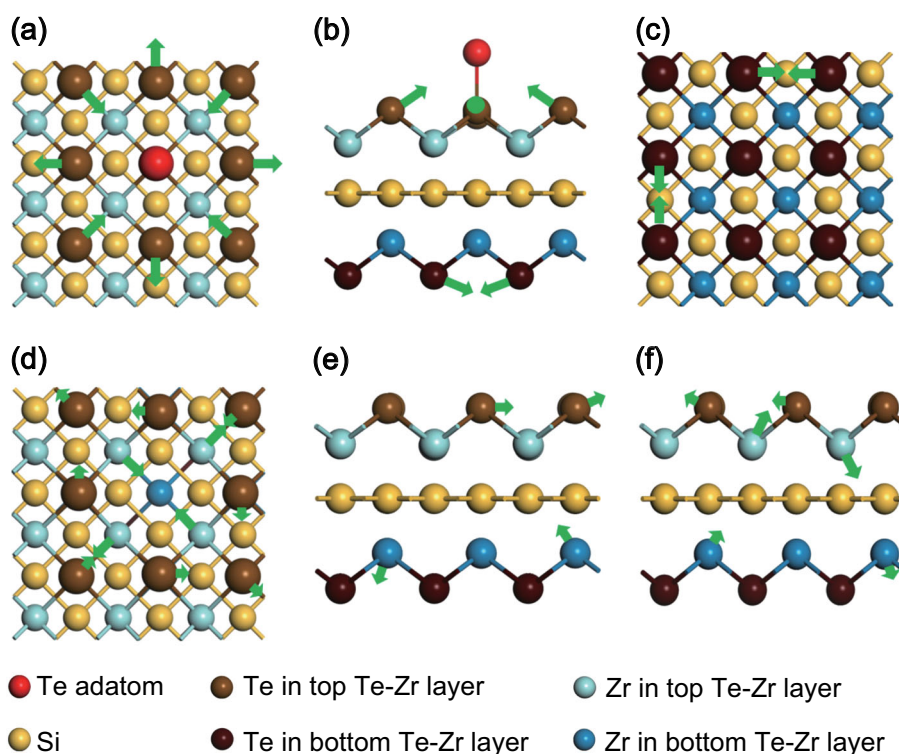


Fig. 4 Vibrational displacements of two defect-induced Raman modes. **a–c** Top, front and bottom view of the vibration modes induced by a Te adatom at 122.2 cm^{-1} and **b–f** Top view, front view and right view of the vibration modes induced by a Te vacancy at 142.9 cm^{-1} , respectively, as shown in a 3×3 1L ZrSiTe lattice

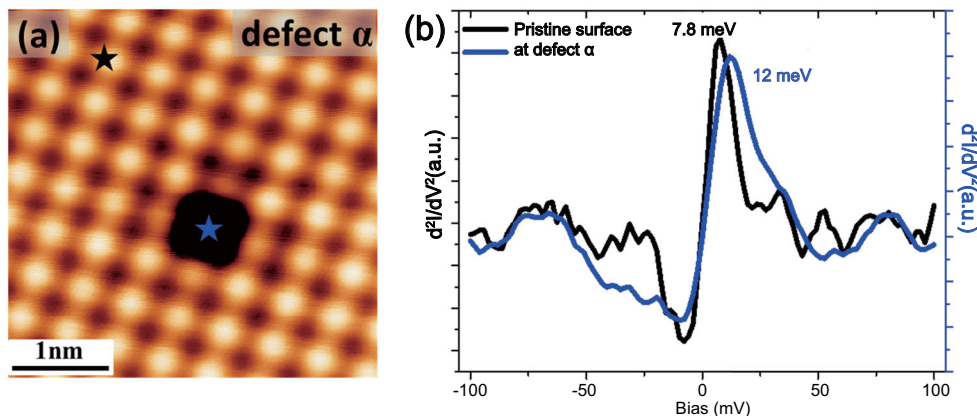


Fig. 5 The secondary differential conductance spectroscopy of defect α . **a** STM image for defect α and **b** the secondary differential conductance (d^2I/dV^2) spectroscopy taken on the defect α (blue) and the pristine surface (black), respectively. The length of the scale bar in **a** is 10 nm

since these defects also exist in as-prepared samples, which calls for a control experiment.

An environment-controlled experiment was carried out to study the effects of degradation of ZrSiTe thin films. We kept the samples in a nitrogen gas-filled glove box, isolated from oxygen and moisture. After one-week storage in the glove box, the Raman spectra of ZrSiTe mono- and few-layers show marked variations. Figure 2c shows the thickness dependence of Raman spectra of the ZrSiTe thin films after one-week storage. For the monolayer, the intensity of the 131.7 cm^{-1} mode is enhanced by 4.8 times and the full width at half maximum (FWHM) is 2.04 times that of a fresh-cleaved ZrSiTe monolayer, which indicates a higher density of defects in the long-stored monolayer. An appreciable red-shift of this mode was also observed after the one-week storage. Our calculation reveals that several defect-induced localized modes exist around 120 cm^{-1} . Here, we show the vibration displacements of a mode at 122.2 cm^{-1} in Fig. 4a–c as an example, which is induced by a Te adatom in the monolayer. More defect-induced localized modes are illustrated in Fig. S2c–j. In addition, the phonons between the X and M points can be involved in Raman scattering processes via defect mediation, and activate the rumpling modes. The energy of these phonons is slightly lower than the ones at the X point. Given that the Raman signal around 131.7 cm^{-1} is a combination of the intralayer shear mode and the defect-induced localized modes, the red-shifts indicate an increasing weight of the localized modes. On the other hand, the A_{1g}^1 and B_{1g}^1 modes are strongly weakened, which most likely result from inversion symmetry breaking in the perpendicular direction because of the defects generated on the topmost Te layer.

In the ZrSiTe few-layers, modes A_{1g}^2 , A_{1g}^1 , and B_{1g}^1 are still dominant. However, the 131.7 cm^{-1} mode disappears and a rather wide peak consisting of several different modes fades in at around 150 cm^{-1} . All these emerging modes are also results of various kinds of defects. Figure 4d–f illustrates the vibrational displacements of a Te vacancy induced local mode at 142.7 cm^{-1} and Fig. S3 summarizes other defect-induced Raman-active vibrational modes near 150 cm^{-1} . The absence of the 131.7 cm^{-1} mode in ZrSiTe few-layers could be, most likely, understood by the scenario that the increasing of interlayer interactions with increasing layer thickness stabilize the ZrSiTe crystalline structure and suppress the layer rumpling motions. And the arising of 143.6 cm^{-1} modes could be ascribed to the Te vacancies.

Degradation of the samples was further investigated with X-ray photoelectron spectroscopy (XPS). Detailed experiment results are discussed in Fig. S6. It is clear that roughly one third of the surface

Te atoms degraded during a two-week storage in the glove box. It is, thus, reasonable to presume that after one-week storage in N_2 atmosphere, a significant number of Te defects appear in the ZrSiTe thin films and the defect-induced mode at 143.6 cm^{-1} arises afterwards.

In order to confirm these defect-induced vibrational modes, we acquired the secondary differential conductance (d^2I/dV^2) spectra at defect α and on the pristine surface, as shown in Fig. 5. Such inelastic tunneling spectroscopy (IETS) has been used to detect the surface phonon modes, for instance, on Au(111) surface⁴⁷. The vibrational spectrum taken on Au(111) shows the symmetric maxima centered at an energy of around $\pm 9\text{ meV}$, well within the energy range of phonons on the Au(111) surface⁴⁷. A giant phonon-mediated inelastic tunneling process ($63 \pm 2\text{ meV}$) was also found in graphene by d^2I/dV^2 spectra⁴⁸. In our case, a symmetric-placed pair of peak/dip at $\pm 7.8\text{ meV}$ is also observed on the pristine surface, as shown in Fig. 5b. At the location of defect α , the vibrational energy increases to $\pm 12\text{ meV}$. According to our DFT calculation, 7.8 (62.9 cm^{-1}) and 12 meV (96.8 cm^{-1}) are corresponding to the energy of the in-plane E_{2g} mode (Fig. S2a) and the Te vacancy-induced intralayer modes (Fig. S4), respectively, which is decided by the selection rules of inelastic tunneling processes. The surface phonon and point-defect-induced phonon modes measured by our IETS agree quite well with the Raman spectra and the DFT calculations, which directly evidence the existence of defect-induced phonon modes. In order to further investigate the structural and symmetry evolution of ZrSiTe few-layers as a function of temperature, we did temperature-dependent Raman measurement and it is clear that no significant crystal phase transition happens during the cooling down despite of consistent stiffening and strengthening of the Raman modes (see Supplementary Information Fig. S5).

To confirm the reproducibility of the thickness dependence of ZrSiTe Raman spectra, we did a Raman mapping over a ZrSiTe flake with its thickness varying from monolayer to four layers. Figure 6 shows intensity maps of the representative Raman peaks over the ZrSiTe flake. The monolayer region can be clearly identified where the 131.7 and 143.6 cm^{-1} signals are significant (bottom-right corner of the sample), whereas the other four modes appear in thicker regions but show nearly no intensity in the monolayer region. The 131.7 cm^{-1} mode could also be seen in the bilayer region in the bottom-left corner with much lower intensity. These results support our assessment that the 131.7 cm^{-1} mode is related to the Te adatoms which exhibit a much higher concentration in the ZrSiTe monolayer. We could also identify signals of the 143.6 cm^{-1} mode at some spots along the edge of the ZrSiTe bilayer, which is consistent with the trend

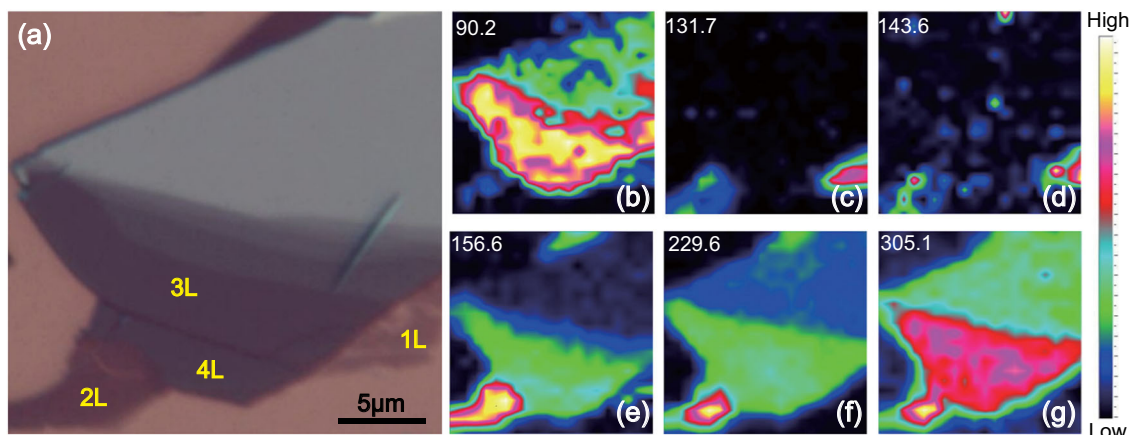


Fig. 6 Intensity mapping of Raman scattering over a ZrSiTe flake. **a** The optical image of a ZrSiTe flake with various thicknesses spreading over its area. The length of the scale bar in the optical image is 5 μm . **b–g** Intensity maps of six Raman modes which can be observed in the sample. The monolayer can be clearly identified in the intensity map of the defect related modes at 131.7 and 143.6 cm^{-1} . Generally, the intensity of Raman scattering decreases with the increasing thickness of ZrSiTe from 2L to higher, as shown in the map of the A_{1g}^1 and B_{1g}^1 modes

that the edges of ZrSiTe thin films are more suspect to be defective. Moreover, the highest intensity of the two characteristic Raman modes (A_{1g}^1 and B_{1g}^1) appears on the bilayer region located at the bottom-left corner of the map. In addition, in the center of the map, three-layered ZrSiTe shows higher Raman intensity than the thicker surrounding areas, which is consistent with the results that thinner ZrSiTe shows stronger Raman signals.

In summary, we have performed a systematic investigation on the Raman-activated vibrational modes in ZrSiTe mono- and few-layers by combining Raman spectroscopy, STM and DFT calculations. We observed three representative Raman modes located at 95 (A_{1g}^2), 228 (A_{1g}^1), and 304 cm^{-1} (B_{1g}^1) in all thicknesses. Exceptionally, single-atom point defects activate BZ edge modes around 130 cm^{-1} and induce localized defect modes near 120 or 150 cm^{-1} . The edge modes were assigned to intralayer shear modes near the BZ edge, corresponding to the surface rumpling of the layers, which is most significant in the monolayer but severely suppressed in thicker layers. The localized modes near 120 cm^{-1} are believed to be a fingerprint of Te adatoms. Their signals are negligible in freshly prepared samples, however, the longer the sample is stored, the stronger their Raman intensity shows and the poorer the vertical symmetry of the layer holds; which results in an appreciable red-shift of the edge modes. All these results evidence that Raman spectroscopy is able to observe some ‘forbidden’ modes in 2D materials, owing to defect-mediated scattering in the q -space or defect-induced local vibrational modes, which allows the detection of various single-atom point defects in metallic layers.

METHODS

Sample preparation and Raman measurements

ZrSiTe single crystals were prepared using a chemical vapor transport method. The stoichiometric mixture of Zr, Si and Te powder was sealed in a quartz tube with iodine used as transport agent (2 mg cm^{-3}). Plate-like single crystals with metallic luster can be obtained via the vapor transport growth with a temperature gradient from 950 to 850 $^{\circ}\text{C}$. The mono- to few-layer ZrSiTe films were achieved by mechanical exfoliation with the Scotch[®] magic tape in a glove box in N_2 atmosphere. During the whole experiment process, the water and oxygen rate was kept below 1 ppm in the glove box. The ZrSiTe thin films were transferred onto the 285 nm SiO_2/Si substrate. And a microscope was used to locate the flakes. Then the samples were kept in covered chip holders in the glove box before further measurements. The samples were transferred into aluminum sample boxes with a glass window that are sealed by rubber O-rings before they were taken out of the glove box for Raman spectroscopic measurement. The Raman spectroscopy was performed with a Horiba Jobin Yvon[®] LabRAM

HR800 confocal Raman microscopy. The system is equipped with a Nd:YAG laser (wavelength 532 nm), a 1800 g mm^{-1} grating, and a Nikon $\times 50$ (NA = 0.5) long-working-distance objective lens. The laser spot size on the sample is close to 1 μm and the spectral resolution is $\approx 0.55 \text{ cm}^{-1}$. Each spectrum was acquired with an integration time of 8 seconds. Such experimental conditions are identical for all spectral measurements. For polarized Raman measurements, the cross-polarization configuration was used. A half-wave plate was placed in the incident laser path to rotate the polarization of the laser. During the room temperature Raman measurement, the samples were kept in the sealed aluminum sample boxes. And the measurement was performed soon after the location of the ZrSiTe films was identified, normally within 1 h after the films were exfoliated from the bulk crystal. The light went through the glass window and focused on the sample surface to get clear signals from the ZrSiTe thin films. A 532 nm laser was used as the activation light and the laser power was 5 mW during the experiment. For the temperature-dependent Raman measurement, the sample was loaded into the special sample holder used for the measurement as soon as it was taken out from the sealed sample box to eliminate the exposure of the samples to the air. All the samples were stored in a covered sample box in the glove box when they were not used for measurement. A Bruker[®] Dimension Edge AFM was used to determine the thickness of ZrSiTe thin film. The STM image was captured with a Unisoku STM system. A bulk ZrSiTe crystal with typical $0.5 \times 2 \text{ mm}^2$ size was attached to the sample holder and the cleavage was done in-situ after the system was pumped to a vacuum better than 1×10^{-10} Torr and cooled down to 4.3 K.

Theoretical methods

DFT calculations were performed using the generalized gradient approximation for the exchange-correlation potential, the projector augmented wave method^{49,50} and a plane-wave basis set as implemented in the Vienna ab-initio simulation package (VASP)^{51–53}, and Quantum Espresso (QE)⁵⁴. DFPT was employed to calculate phonon-related properties, including Raman intensity (QE), activity (QE) and shifts (VASP), vibrational frequencies at the Gamma point (VASP) and other vibration-related properties (VASP). The kinetic energy cut-off for the plane-wave basis set was set to 700 eV for geometric and vibrational properties for primitive cells from 1 to 4L and 550 eV for the calculations of 3×3 1L supercells with defects. A k -mesh of $20 \times 20 \times 1$ was adopted to sample the first Brillouin zone of the conventional unit cell of the few-layers and a $6 \times 6 \times 1$ k -mesh was used for the $3 \times 3 \times 1$ supercell. A Gaussian smearing of 0.05 eV was used in our calculations. In optimizing the system geometry and vibration calculations, van der Waals (vdW) interactions were considered at the vdW-DF^{55,56} level with the optB86b exchange functional (optB86b-vdW)^{57–59}, which was proved to be accurate in describing the structural properties of layered materials^{27,37,60,61}. The shape and volume of each supercell were fully optimized and all atoms in the supercell were allowed to relax until the residual force per atom was less than $1 \times 10^{-3} \text{ eV \AA}^{-1}$. The electronic band structure is calculated using Perdew–Burke–Ernzerhof (PBE) functional with spin–orbit coupling (SOC)⁶².

A 6×6 1L supercell was used for the STM simulation with the 400 eV energy cut-off and $2 \times 2 \times 1$ k -point mesh. The defect-deformation energy ΔE_i was induced to explain the concentration difference of the three types of defects. The defect-deformation energy can be defined as⁶³

$$\Delta E = E_i(\text{defect}) - E(\text{supercell}) + \sum_{s=1}^{N_{\text{species}}} n_s^i \mu_s$$

$E_i(\text{defect})$ is the total energy of the system with defect while the E (supercell) is the total energy of the supercell without defect. The n_s^i means the number of the atoms of the s defect: this parameter is negative to adatoms and is positive to vacancies. The μ_s is the chemical potential of the s defect. Considering it is difficult to obtain the exact value of μ_s , the system was assumed to vary between two limiting cases: tellurium-rich [$\mu_{\text{Te}} = \mu_{\text{Te}}^*$ and $\mu_{\text{Zr}}^* + \Delta H < \mu_{\text{Zr}} < \mu_{\text{Zr}}^*$, where μ_{Te}^* is the chemical potential of Te in the α -phase crystal form, μ_{Zr}^* is the chemical potential of Zr in the bulk form and ΔH is the formation enthalpy of ZrSiTe] and zirconium-rich (tellurium-deficient) [$\mu_{\text{Zr}} = \mu_{\text{Zr}}^*$ and $\mu_{\text{Te}}^* + \Delta H < \mu_{\text{Te}} < \mu_{\text{Te}}^*$]. The 3×3 bilayer supercell was used to calculate the defect-deformation energy.

Vibrational frequencies and polarization vectors at the Brillouin zone center were calculated using the DFPT. In a rigid-layer vibrational mode, the whole layer can be treated as one rigid body^{64,65}. The projected interlayer force constant (p-ILFC) k^i (i stands for the projected direction, e.g., x , y , or z) was constructed by summing inter-atomic force constants over all atoms from each of the two adjacent layers, as $k_{AB}^i = \sum_{a,b} D_{a,b}^i$ ($a \in [\text{atoms in layer A}]$, $b \in [\text{atoms in layer B}]$). The matrix of

inter-atomic force constants, essentially the same as the Hessian matrix of Born–Oppenheimer energy surface, is defined as the energetic response to a distortion of atomic geometry in DFPT⁶⁶. It reads, $D_{a,b}^i = \frac{\partial^2 E(R)}{\partial R_a^i \partial R_b^i}$, where R is the coordinate of each ion, $E(R)$ is the ground-state energy. The force on an individual ion can thus be expressed to $F_i = -\frac{\partial E(R)}{\partial R^i}$. Vibrational frequency ω are related to the eigenvalues of the Hessian matrix and atomic masses. It reads $\det \left| \frac{1}{4m^2 c^2} \frac{D_{a,b}^i}{m_{a,b}} - \omega^2 \right| = 0$, where $m_{a,b}$ is the effective mass, defined as $\sqrt{m_a m_b}$.

DATA AVAILABILITY

The data used in this study are available upon reasonable request from the corresponding author M.H.P. (minghupan@hust.edu.cn).

ACKNOWLEDGEMENTS

Raman and STM measurements were conducted by H.Y., Y.C., and M.P. at School of Physics, Huazhong University of Science and Technology in Wuhan. This work is financially supported by National Natural Science Foundation of China (Project Codes 11574095, 11604106, 11622437, and 61674171), the Strategic Priority Research Program of Chinese Academy of Sciences (Grant No. XDB30000000), and the Fundamental Research Funds for the Central Universities of China and the Research Funds of Renmin University of China (Grant Nos. 16XNLQ01 and 19XNH065). Sample growth was carried out by J.H., Y.Z., and Z.M. in Tulane University, LA, supported by the US Department of Energy under Grant No. DE-SC0014208. Calculations were performed at the Physics Lab of High-Performance Computing of Renmin University of China.

AUTHOR CONTRIBUTIONS

H.Y., X.Z., and Y.C. contributed equally to this manuscript. H.Y., Y.C., and M.H.P. carried out Raman and STM measurements. X.Z. and W.J. performed the DFT and DFT simulations. J.H., Y.Z., and Z.M. grew the crystals. All authors analyzed the experimental and calculated data and wrote the paper. W.J. and M.P. supervised the project.

ADDITIONAL INFORMATION

Supplementary Information accompanies the paper on the *npj 2D Materials and Applications* website (<https://doi.org/10.1038/s41699-019-0093-7>).

Competing interests: The authors declare no competing interests.

Publisher's note: Springer Nature remains neutral with regard to jurisdictional claims in published maps and institutional affiliations.

REFERENCES

- Fang, C., Chen, Y., Kee, H.-Y. & Fu, L. Topological nodal line semimetals with and without spin-orbital coupling. *Phys. Rev. B* **92**, 081201 (2015).
- Yang, B.-J., Bojesen, T. A., Morimoto, T. & Furusaki, A. Topological semimetals protected by off-centered symmetries in nonsymmorphic crystals. *Phys. Rev. B* **95**, 075135 (2017).
- Fang, C., Weng, H., Dai, X. & Zhong, F. Topological nodal line semimetals. *Chin. Phys. B* **25**, 117106 (2016).
- Bensch, W. & Durichen, P. Structure of the layer compound ZrSiTe. *Acta Crystallogr. Sect. C* **50**, 346–348 (1994).
- Hosen, M. M. et al. Tunability of the topological nodal-line semimetal phase in ZrSiX-type materials (X=S, Se, Te). *Phys. Rev. B* **95**, 161101 (2017).
- Neupane, M. et al. Observation of topological nodal fermion semimetal phase in ZrSiS. *Phys. Rev. B* **93**, 201104 (2016).
- Schoop, L. M. et al. Dirac cone protected by non-symmorphic symmetry and three-dimensional Dirac line node in ZrSiS. *Nat. Commun.* **7**, 11696 (2016).
- Hu, J. et al. Evidence of topological nodal-line fermions in ZrSiSe and ZrSiTe. *Phys. Rev. Lett.* **117**, 016602 (2016).
- Xu, Q. et al. Two-dimensional oxide topological insulator with iron-pnictide superconductor LiFeAs structure. *Phys. Rev. B* **92**, 205310 (2015).
- Young, S. M. & Kane, C. L. Dirac semimetals in two dimensions. *Phys. Rev. Lett.* **115**, 126803 (2015).
- Ferrari, A. C. et al. Raman spectrum of graphene and graphene layers. *Phys. Rev. Lett.* **97**, 187401 (2006).
- Graf, D. et al. Spatially resolved raman spectroscopy of single- and few-layer graphene. *Nano Lett.* **7**, 238–242 (2007).
- Ataca, C., Topsakal, M., Aktürk, E. & Ciraci, S. A comparative study of lattice dynamics of three- and two-dimensional MoS₂. *J. Phys. Chem. C* **115**, 16354–16361 (2011).
- Lee, Y.-H. et al. Synthesis of large-area MoS₂ atomic layers with chemical vapor deposition. *Adv. Mater.* **24**, 2320–2325 (2012).
- Li, H. et al. From bulk to monolayer MoS₂: evolution of raman scattering. *Adv. Funct. Mater.* **22**, 1385–1390 (2012).
- Lanzillo, N. A. et al. Temperature-dependent phonon shifts in monolayer MoS₂. *Appl. Phys. Lett.* **103**, 093102 (2013).
- Gutiérrez, H. R. et al. Extraordinary room-temperature photoluminescence in triangular WS₂ monolayers. *Nano Lett.* **13**, 3447–3454 (2012).
- Yamamoto, M. et al. Strong enhancement of raman scattering from a bulk-inactive vibrational mode in few-layer MoTe₂. *ACS Nano* **8**, 3895–3903 (2014).
- Guo, H. et al. Double resonance Raman modes in monolayer and few-layer MoTe₂. *Phys. Rev. B* **91**, 205415 (2015).
- Jana, M. K. et al. A combined experimental and theoretical study of the structural, electronic and vibrational properties of bulk and few-layer Td-WTe₂. *J. Phys.* **27**, 285401 (2015).
- Liu, H. et al. Phosphorene: an unexplored 2D semiconductor with a high hole mobility. *ACS Nano* **8**, 4033–4041 (2014).
- Shi, W. et al. Raman and photoluminescence spectra of two-dimensional nanocrystallites of monolayer WS₂ and WSe₂. *2D Mater.* **3**, 025016 (2016).
- Wu, J.-B. et al. Monolayer molybdenum disulfide nanoribbons with high optical anisotropy. *Adv. Opt. Mater.* **4**, 756–762 (2016).
- Ribeiro, H. B. et al. Edge phonons in black phosphorus. *Nat. Commun.* **7**, 12191 (2016).
- Guo, Y. et al. Discovering the forbidden Raman modes at the edges of layered materials. *Sci. Adv.* **4**, eaau6252 (2018).
- Richter, H., Wang, Z. P. & Ley, L. The one phonon Raman spectrum in microcrystalline silicon. *Solid State Commun.* **39**, 625–629 (1981).
- Hong, J. et al. Exploring atomic defects in molybdenum disulfide monolayers. *Nat. Commun.* **6**, 6293 (2015).
- He, Y.-M. et al. Single quantum emitters in monolayer semiconductors. *Nat. Nanotechnol.* **10**, 497 (2015).
- Zhang, S. et al. Defect structure of localized excitons in a WSe₂ monolayer. *Phys. Rev. Lett.* **119**, 046101 (2017).
- Bensch, W., Dürichen, P., Helmer, O., Reller, A. & Sazama, U. Metal selective redox processes in the ternary compound ZrSiTe. *Inorg. Chim. Acta* **252**, 47–53 (1996).
- Cao, Y. et al. Anomalous vibrational modes in few layer WTe₂ revealed by polarized Raman scattering and first-principles calculations. *2D Mater.* **3**, 035024 (2017).
- Jiang, Y. C., Gao, J. & Wang, L. Raman fingerprint for semi-metal WTe₂ evolving from bulk to monolayer. *Sci. Rep.* **6**, 19624 (2016).
- Gupta, A., Chen, G., Joshi, P., Tadigadapa, S. & Eklund, P. C. Raman scattering from high-frequency phonons in supported n-graphene layer films. *Nano Lett.* **6**, 2667–2673 (2006).
- Chakraborty, B., Matte, H. S. S. R., Sood, A. K. & Rao, C. N. R. Layer-dependent resonant Raman scattering of a few layer MoS₂. *J. Raman Spectrosc.* **44**, 92–96 (2013).

35. Li, S.-L. et al. Quantitative raman spectrum and reliable thickness identification for atomic layers on insulating substrates. *ACS Nano* **6**, 7381–7388 (2012).
36. Kim, J. et al. Anomalous polarization dependence of Raman scattering and crystallographic orientation of black phosphorus. *Nanoscale* **7**, 18708–18715 (2015).
37. Hu, Z.-X., Kong, X., Qiao, J., Normand, B. & Wei, J. Interlayer electronic hybridization leads to exceptional thickness-dependent vibrational properties in few-layer black phosphorus. *Nanoscale* **8**, 2740–2750 (2016).
38. Du, Y. et al. One-dimensional van der Waals material tellurium: Raman spectroscopy under strain and magneto-transport. *Nano Lett.* **17**, 3965–3973 (2017).
39. Pine, A. S. & Dresselhaus, G. Raman spectra and lattice dynamics of tellurium. *Phys. Rev. B* **4**, 356–371 (1971).
40. Qiao, J. et al. Few-layer tellurium: one-dimensional-like layered elementary semiconductor with striking physical properties. *Sci. Bull.* **63**, 159–168 (2018).
41. Ye, F. et al. Environmental instability and degradation of single- and few-layer WTe₂ nanosheets in ambient conditions. *Small* **12**, 5802–5808 (2016).
42. Julien, C. et al. Resonant Raman scattering studies of SnS₂ crystals. *Mater. Sci. Eng. B* **23**, 98–104 (1994).
43. Cingolani, A., Ferrara, M., Lugar, M. & Levy, F. The Raman spectra of CdI₂. *Solid State Commun.* **50**, 911–913 (1984).
44. O'Brien, M. et al. Raman characterization of platinum diselenide thin films. *2D Mater.* **3**, 021004 (2016).
45. Roubi, L. & Carlone, C. Resonance Raman spectrum of HfS₂ and ZrS₂. *Phys. Rev. B* **37**, 6808–6812 (1988).
46. Yan, M. et al. High quality atomically thin PtSe₂ films grown by molecular beam epitaxy. *2D Mater.* **4**, 045015 (2017).
47. Gawronski, H., Mehlhorn, M. & Morgenstern, K. Imaging phonon excitation with atomic resolution. *Science* **319**, 930–933 (2008).
48. Zhang, Y. et al. Giant phonon-induced conductance in scanning tunnelling spectroscopy of gate-tunable graphene. *Nat. Phys.* **4**, 627–630 (2008).
49. Blöchl, P. E. Projector augmented-wave method. *Phys. Rev. B* **50**, 17953–17979 (1994).
50. Kresse, G. & Joubert, D. From ultrasoft pseudopotentials to the projector augmented-wave method. *Phys. Rev. B* **59**, 1758–1775 (1999).
51. Kresse, G. & Hafner, J. Ab initio molecular dynamics for liquid metals. *Phys. Rev. B* **47**, 558–561 (1993).
52. Furthmüller, J. & Kresse, G. Efficient iterative schemes for ab initio total-energy calculations using a plane-wave basis set. *Phys. Rev. B* **54**, 11169 (1999).
53. Kresse, G. & Furthmüller, J. Efficiency of ab-initio total energy calculations for metals and semiconductors using a plane-wave basis set. *Comput. Mater. Sci.* **6**, 15–50 (1996).
54. Giannozzi, P. et al. QUANTUM ESPRESSO: a modular and open-source software project for quantum simulations of materials. *J. Phys. Condens. Matter.* **21**, 395502 (2009).
55. Dion, M., Rydberg, H., Schröder, E., Langreth, D. C. & Lundqvist, B. I. Van der Waals density functional for general geometries. *Phys. Rev. Lett.* **92**, 246401 (2004).
56. Lee, K., Murray, E. D., Kong, L., Lundqvist, B. I. & Langreth, D. C. Higher-accuracy van der Waals density functional. *Phys. Rev. B* **82**, 081101 (2010).
57. Klimes, J., Bowler, D. R. & Michaelides, A. Chemical accuracy for the van der Waals density functional. *J. Phys.* **22**, 022201 (2010).
58. Klimeš, J., Bowler, D. R. & Michaelides, A. Van der Waals density functionals applied to solids. *Phys. Rev. B* **83**, 195131 (2011).
59. Thonhauser, T. et al. Van der Waals density functional: self-consistent potential and the nature of the van der Waals bond. *Phys. Rev. B* **76**, 125112 (2007).
60. Qiao, J., Kong, X., Hu, Z.-X., Yang, F. & Ji, W. High-mobility transport anisotropy and linear dichroism in few-layer black phosphorus. *Nat. Commun.* **5**, 4475–4481 (2014).
61. Zhao, Y. et al. High electron mobility and air stable 2D layered PtSe₂ FETs. *Adv. Mater.* **29**, 1604230 (2017).
62. Oba, F., Togo, A., Tanak, I., Paier, J. & Kress, G. Defect energetics in ZnO: a hybrid Hartree-Fock density functional study. *Phys. Rev. B* **77**, 245202 (2008).
63. Perdew, J. P., Burke, K. & Ernzerhof, M. Generalized gradient approximation made simple. *Phys. Rev. Lett.* **77**, 3865–3868 (1996).
64. Verble, J. L., Wietling, T. J. & Reed, P. R. Rigid-layer lattice vibrations and van der Waals bonding in hexagonal MoS₂. *Solid State Commun.* **11**, 941–944 (1972).
65. Zhao, Y. et al. Extraordinarily strong interlayer interaction in 2D layered PtS₂. *Adv. Mater.* **28**, 2399–2407 (2016).
66. Baroni, S., de Gironcoli, S., Dal Corso, A. & Giannozzi, P. Phonons and related crystal properties from density-functional perturbation theory. *Rev. Mod. Phys.* **73**, 515–562 (2001).



Open Access This article is licensed under a Creative Commons Attribution 4.0 International License, which permits use, sharing, adaptation, distribution and reproduction in any medium or format, as long as you give appropriate credit to the original author(s) and the source, provide a link to the Creative Commons license, and indicate if changes were made. The images or other third party material in this article are included in the article's Creative Commons license, unless indicated otherwise in a credit line to the material. If material is not included in the article's Creative Commons license and your intended use is not permitted by statutory regulation or exceeds the permitted use, you will need to obtain permission directly from the copyright holder. To view a copy of this license, visit <http://creativecommons.org/licenses/by/4.0/>.

© The Author(s) 2019